Coupling-Assisted Renormalization of Excitons and Vibrations in Compressed MoSe₂−WSe₂ Heterostructure

Xinpeng Fu,[†] Fangfei Li,*[†] Jung-Fu Lin,[‡] Yuanbo Gong,[†] Xiaoli Huang,[†] Yanping Huang,[†] Hanxue Gao,[†] Qiang Zhou,*[†] and Tian Cui[†]

[†]State Key Laboratory of Superhard Materials, College of Physics, Jilin University, Changchun 130012, China
[‡]Department of Geological Sciences, The University of Texas at Austin, Austin, Texas 78712, United States

S *Supporting Information*

ABSTRACT: Vertical heterostructures (HSs) constructed with two-dimensional (2D) materials is expected to generate fascinating properties due to interlayer coupling between neighboring layers. However, interlayer coupling can be easily obscured by cross-contamination during transfer processes, rendering their experimental demonstration challenging. Here, we explore the coupling-assisted renormalization of excitons and vibrations in a mechanically fabricated MoSe₂−WSe₂ HS through high-pressure photoluminescence, Raman spectra, and density functional theory calculations. Accompanied by the interlayer coupling enhancement, the excitonic and vibrational renormalizations involving dimensionality and composition variations were achieved. A cycle of 2D−3D−2D excitonic evolution was disclosed and pressure-induced emergence of X⁻ exciton of MoSe₂ in HS was found reflecting the band structure transition in the MoSe₂−WSe₂ HS. The Raman spectra reveals that the coupled A₂″ vibrations of WSe₂ and MoSe₂ in HS was stiffened and out-of-plane A₁′ vibrations of WSe₂ and MoSe₂ in HS got coherent upon pressure modulation. This coupling-assisted renormalization in MoSe₂−WSe₂ HS can be extended to other 2D layered HSs, which indicates the possibility to design a flexible HS with controlled excitonic and vibrational system for light-emitting diodes, excitonic, and photovoltaic devices.
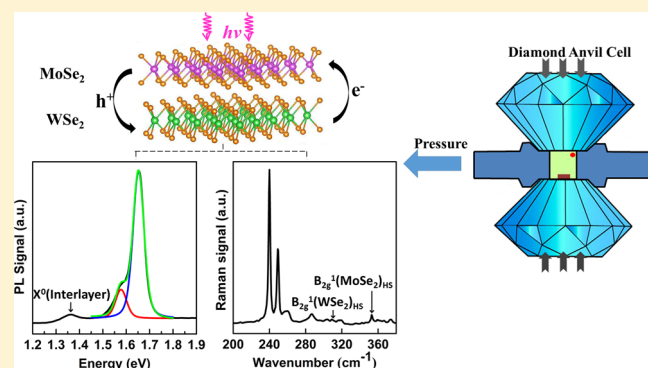
■ INTRODUCTION

Transition metal dichalcogenides (TMDs) 2H-MX₂ (M = Mo, W, etc., X = S, Se, and Te) have received considerable interests in recent years due to their excellent optical and electronic properties.[1−3] In natural bulk 2H-MX₂, many alternating sandwiched X−M−X layers are loosely coupled to each other by van der Waals (vdW) forces. Due to the effect of the interlayer coupling,[4−6] optical properties of TMDs can be tuned largely by varying the atomic thickness.[7,8] A strong photoluminescence (PL) can be obtained by thinning down bulks to monolayers due to the consequent indirect to direct band gap transition process in TMDs, which gives rise to many potential applications in optoelectronics.[9−15] Because the large binding energy exists in these two-dimensional (2D) semiconductors, exciton dominates the optical response, exhibiting strong light−matter interactions that are electrically and strained tunable.[16−20] The discovery of excitonic valley physics and pseudospin physics in 2H-TMDs expands device concepts nonexistent in other material systems.[21−27]

Interestingly, utilizing van der Waals interlayer coupling offers the possibility to form vertical TMDs heterostructures (HSs) by stacking different TMD monolayers together.[28−30] One highly coveted is that of differing monolayer MoSe₂ and WSe₂ with type II band alignment. The MoSe₂ and WSe₂ share the approximately same crystalline structure; however, their physical properties such as spin−orbit coupling strength, band gap, and exciton resonance vary significantly. Particularly, their distinct well-separated excitonic features are available to explore excitonic physics and functionalities of vertically stacked monolayer TMDs HSs. The energy band structure of MoSe₂−WSe₂ HS is renormalized by the interlayer coupling effect, which can lead to a crossover from a 2D excitonic system in the monolayer to a three-dimensional (3D) excitonic system in the HSs. The 3D excitonic system possesses concomitant 2D intralayer excitons of contributing monolayers and 3D interlayer exciton that is formed by bound hole and electron localized in individual monolayers. Controlling of the interlayer coupling signifies the ability of effectively modulating the quantity, energy, and even dimensionality of the exciton in HSs; it is significant to give insight into the low-dimensional physics, and discover new phenomena with rich functionalities and novel physical effects.

In addition to the excitonic explorations on HS, seeking electronic band structure renormalization, the vibrational explorations are necessary to demonstrate their lattice structure renormalization, elaborating on the structural stability, and

A
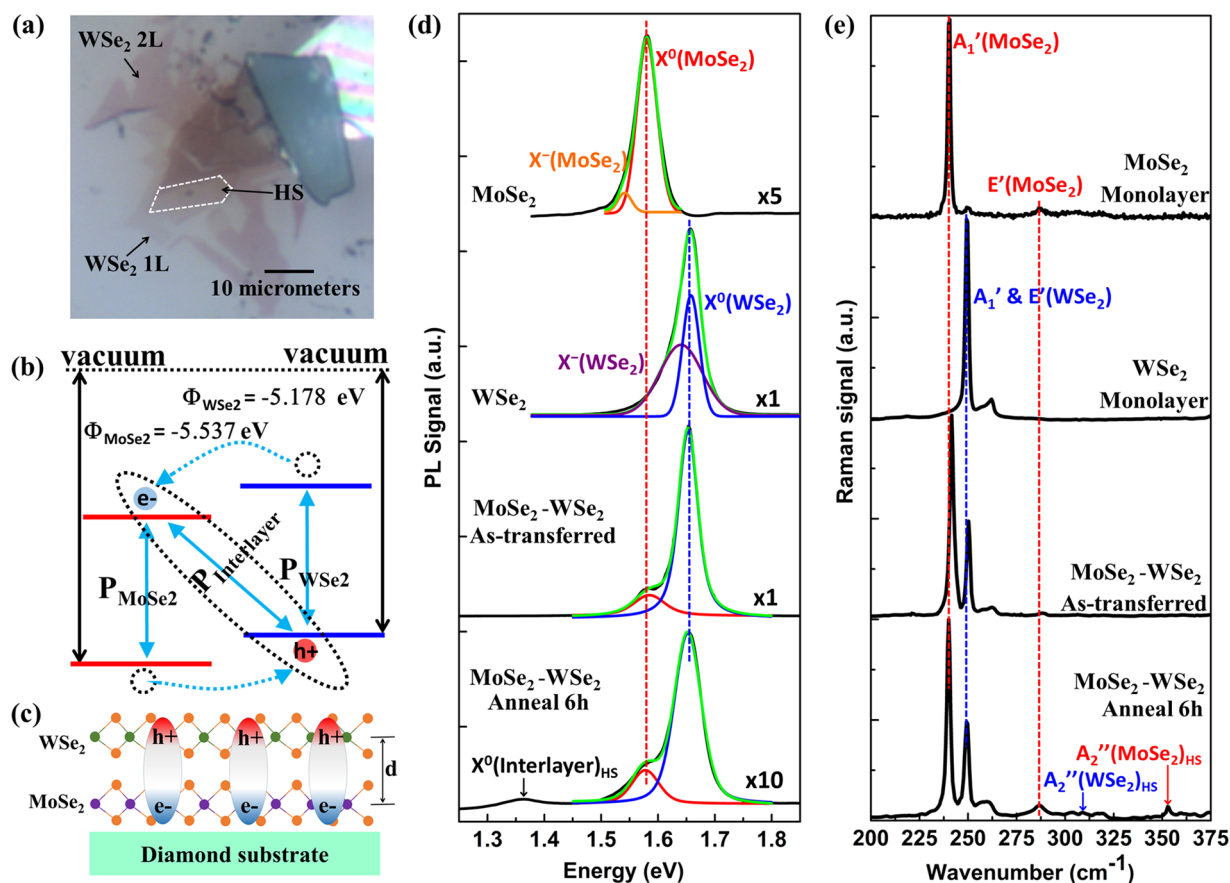
Figure 1. (a) Microscopy image of $MoSe_2$−WSe_2 HS; the area of HS are marked with a white dashed line. (b) Band alignment of $MoSe_2$−WSe_2 HS from first-principles calculations with work functions 5.537 and 5.178 eV for $MoSe_2$ and WSe_2, respectively. (c) Schematic diagram of 3D interlayer exciton gas in $MoSe_2$−WSe_2 HS. Room-temperature photoluminescences (d) and Raman spectra (e) of monolayer $MoSe_2$, monolayer WSe_2, and WSe_2−$MoSe_2$ HS before and after the thermal annealing. The dashed lines are guides to the eye. The raw data in (d) were fitted with multi-Gaussian function, and individual components X^0 and X^- emission are displayed in red curves and orange curves for $MoSe_2$, blue curves and purple curves for WSe_2, green curves for overall fitted spectra, respectively. The scaling factor listed on the right side of the corresponding curve represents the ratio of monolayer WSe_2 PL intensity and its own intensity at the same experimental condition.

dimensional crossover. As is reported, the B_{2g}^1 mode that arises from out-of-plane (breathing) vibration has been observed in few-layer TMDs. The B_{2g}^1 mode involves interlayer interaction from restoring force existed in several component layers, and can be regarded as an important criterion for distinguishing monolayer from multilayers.[31−34] The way of stacking in HS causes its symmetry to change to the one similar to homostructural stacking. Indeed, exploring the existence of such vibrational modes and their dependence on the interlayer coupling intensity in an atomic clean HS is attractive and concerned for probing dimensionality effects of 2D materials. As we know, an effective way for tuning the interlayer coupling intensity is to alter the interlayer distance of HS by applying uniaxial, biaxial, or hydrostatic strain. In particular, hydrostatic pressure applied on in-plane and out-of-plane generates diverse compressive strains, it is conducive to revealing unique physical phenomena and realizing an optimized potential of vertically stacked monolayer TMDs HSs in extremes.[18,35,36]

In this work, we investigated the coupling-assisted renormalized excitonic and vibrational evolutions in compressed $MoSe_2$−WSe_2 HS using a diamond anvil cell (DAC) in conjunction with theoretical calculations. Through vacuum annealing process and application of hydrostatic pressure, interlayer coupling was enhanced across the van der Waals gap between neighboring layers, the excitonic system and vibra-

tional motions were renormalized with variations in dimensionality and compositions. The pressure-induced evolutions of interlayer and intralayer excitons energies and Raman vibrational frequencies obtained here hold the potential for developing optoelectronic devices such as p−n junctions and flexible excitonic circuits.

■ RESULTS AND DISCUSSION

Monolayer $1H$-$MoSe_2$ and WSe_2 films were prepared by mechanical exfoliation of bulk crystals (2D Semiconductor supplies) using a Gel Film (Gel-Pak).[37,38] Through the optical contrast, Raman spectroscopy, and PL spectroscopy-based appraisal (Figure 1), the monolayer $MoSe_2$ and WSe_2 processing strong excitonic effect were confirmed, the X^0 and X^- emissions are located at about 1.58 and 1.54 eV for monolayer $MoSe_2$, and about 1.66 and 1.64 eV for monolayer WSe_2 at room condition, which are consistent with previous reports (Figure 1d).[17,19,20] The fact that monolayer WSe_2 owns 5 times higher PL yield than the monolayer $MoSe_2$ indicates a stronger nonradiative recombination in the $MoSe_2$. The flake with a high-quality WSe_2 monolayer region was selectively transferred onto the $MoSe_2$ monolayer to form a $MoSe_2$−WSe_2 HS sample (Figure 1a), followed by mild vacuum annealing (<0.133 Pa, 120 °C, 6 h) to remove redundant interspace (see Experimental Methods and Figure S1). First principles
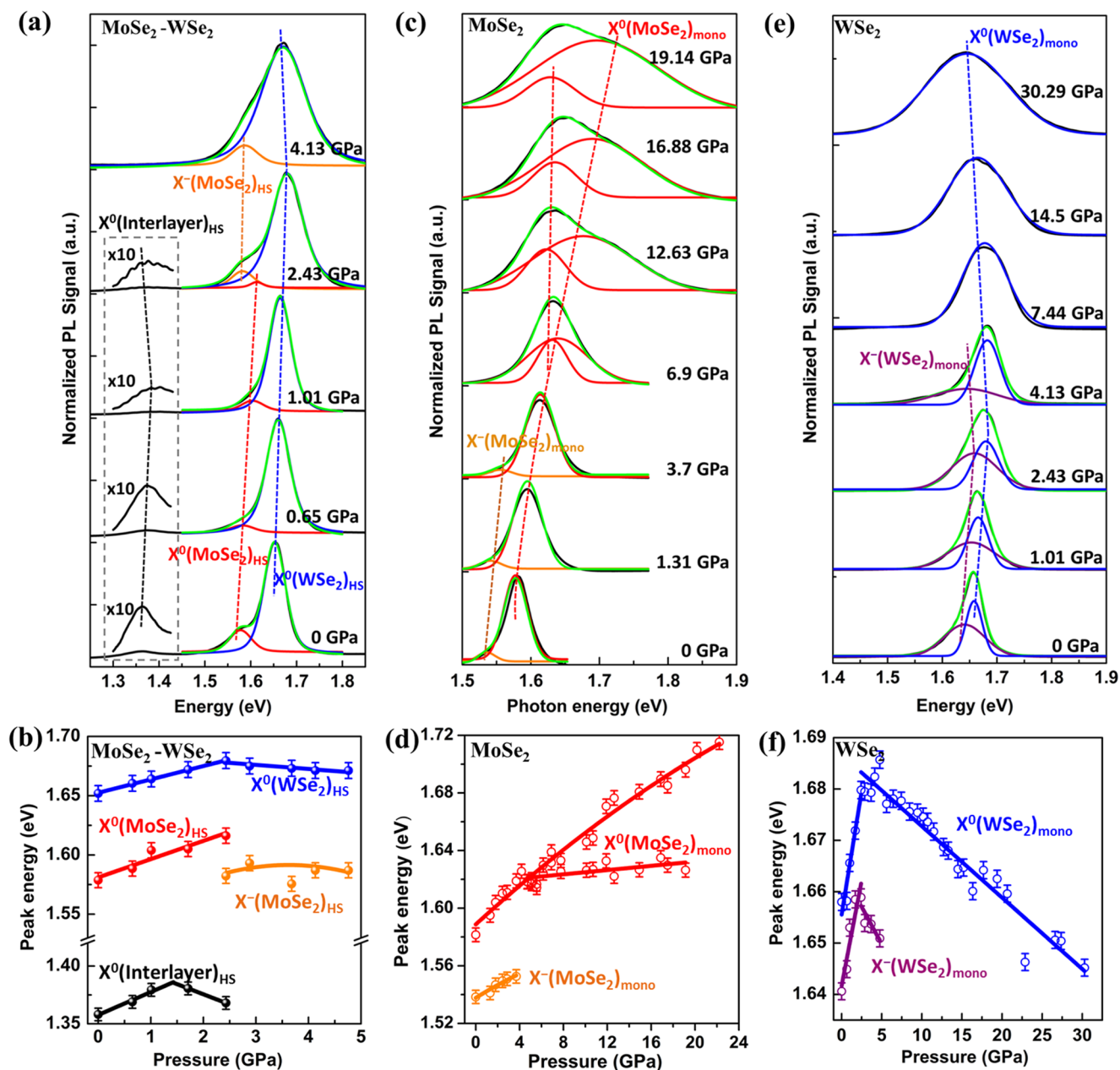
Figure 2. Normalized PL spectra (a) and excitons energy evolutions (b) as a function of pressure for the MoSe$_2$−WSe$_2$ HS; (c) and (d) for monolayer MoSe$_2$; (e) and (f) for monolayer WSe$_2$; color-coded by red (the X^0 exciton emission of MoSe$_2$ in the HS and monolayer), orange (the X$^-$ exciton emission of MoSe$_2$ in the HS and monolayer), blue (the X^0 exciton emission of WSe$_2$ in the HS and monolayer), and purple (the X$^-$ exciton emission of monolayer WSe$_2$). The dashed lines are guides to the eye.

calculation shows that MoSe$_2$−WSe$_2$ HS has a type II band alignment, where the highest valence band and the lowest conduction band lie in WSe$_2$ and MoSe$_2$ layers, respectively. The type II band alignment induces the photoexcited electrons and holes relaxing to the conduction band edge of MoSe$_2$ and the valence band edge of WSe$_2$, respectively (Figure 1b). The interlayer exciton is derived from the Coulombic attraction between electrons in the MoSe$_2$ and holes in the WSe$_2$, which is similar to spatially indirect excitons in coupled quantum wells (Figure 1c).

Before vacuum annealing, the as-transferred HS gives two PL peaks located at ~1.66 and 1.58 eV, consistent with the X^0 exciton emissions of the individual monolayer MoSe$_2$ and WSe$_2$, respectively. It is in a state of "spotty-coupled", namely

an unintentional redundant interspace trapped between the monolayers. This indicates a spatially inhomogeneous HS composed of strongly and weakly coupled regions. Through vacuum annealing, it effectively decreases the redundant interspace trapped between the monolayers, and converts the luminescence spectrum of the HS's from spotty-coupled profile to a new profile assisted with charge transfer and band renormalization, as shown in Figure 1d. The converted state gets a strong electronic coupling in major regions to become a true heterobilayer with the band structure transformation. Employing a multiple-peak fitting to analyze the measured PL spectra, the overall phenomena were summarized as follows:

(1) The PL intensity of WSe$_2$ in the annealed HS is 10 times lower than that of individual WSe$_2$. This pronounced PL

quenching effect suggests that photoexcited electrons in WSe$_2$ transfer to the lower states in MoSe$_2$ instead of forming exciton in WSe$_2$ and recombining radiatively.

(2) A new emission peak located at 1.35 eV emerges, indicating the existence of the interlayer exciton, which originates from Coulombic attraction between electrons in the MoSe$_2$ and holes in the WSe$_2$. This represents the renormalization of excitonic system involving a dimensional transformation from 2D to 3D.

In addition, we mentioned here that the peaks corresponding to the X$^-$ exciton emission of the individual monolayer MoSe$_2$ and WSe$_2$ are not observed for as-transferred HS. On the basis of energy band alignment of the HS, the disappearance of the X$^-$ exciton emission peak of monolayer WSe$_2$ is attributed to the ultrafast charge relaxation across the HS. It involves not only sweeping holes of MoSe$_2$ to WSe$_2$, but also sweeping electrons of WSe$_2$ to MoSe$_2$, which leads to quenching of the X$^-$ emissions in WSe$_2$ across the HS. However, the absence of the X$^-$ exciton emission peak of MoSe$_2$ after electrons sweeping from WSe$_2$ toward MoSe$_2$ is due to an asymmetric behavior in trion emission from MoSe$_2$ and WSe$_2$ layers as a result of different bonding character in the HS.[39] The detailed explanation is displayed in Figure S3. For annealed HS, the X$^-$ exciton emission peak of monolayer WSe$_2$ disappears due to the ultrafast charge relaxation across the HS. The disappearance of the X$^-$ exciton emission peak of monolayer MoSe$_2$ is ascribed to the formation of the interlayer excitons, which consumes lots of electrons of MoSe$_2$.

In the Raman spectra shown in Figure 1e, the out-of-plane A$_1'$ and the in-plane E$'$ vibrations of MoSe$_2$ and WSe$_2$ for the as-transferred HS are well resolved from each monolayers. Due to the dielectric environmental changes during as-transferred HS formation, slight blue-shifts of these two modes are observed. After annealing, two new peaks appear at 352.8 and 308.8 cm^{-1} in the bilayer limit HS, which have never been observed in individual monolayer MoSe$_2$ or WSe$_2$. These vibrations involve a finite restoring force between two component layers, are identified as A$_2''$ modes of WSe$_2$ and MoSe$_2$ in HS. Compared with the excitonic renormalization, the vibrational motions renormalization is found here, revealing that the spotty-coupled status has converted to a true 3D heterobilayer.

As tight-binding theory and quantum tunneling model are expected, the interlayer interaction is expected to be exponentially sensitive to the interlayer distance.[39] Therefore, the way of vacuum annealing effectively reinforces the interlayer coupling, forming interlayer exciton and activating A$_2''$ vibrational modes in the vdW HS. However, this method is confined to noncontinuous reduction in the interlayer distance. Considering that, the employment of hydrostatic pressure is a good choice to achieve a continuous modulation of the interlayer interaction. When a given hydrostatic pressure is applied, the compressive strains will greatly affect the interlayers bond by van der Waals force, accompanied by shortened interlayer distance and enhanced interlayer interactions. On the contrary, the response of intralayers with strong covalent bonds to the tunability of hydrostatic pressure tends to be torpid. Hence, using this method, the further renormalization of excitonic and vibrational systems with enhanced interlayer coupling under pressure can be achieved.

The normalized PL spectra of MoSe$_2$−WSe$_2$ HS as a function of photon energy are shown in Figure 2a (details of the high-pressure experiments are presented in Experimental Methods and Figure S2 in the Supporting Information). The raw data in the panel are fitted with multi-Gaussian functions. The red and blue curves represent individual components X^0 exciton emissions of MoSe$_2$ and WSe$_2$ in HS, and the green curves represent an overall fitted spectra. As indicated by blue dashed lines in Figure 2a, the X^0 emission of WSe$_2$ first exhibits a blue-shift as the pressure increases and then exhibits a linear red-shift above 2.43 GPa. However, the X^0 emission of MoSe$_2$ only shows a nearly linear blue-shift from 0 to 2.43 GPa (red dashed lines). The integrated relative intensity of the X^0 peak of MoSe$_2$ decreases gradually with pressure and almost disappeared up to 2.43 GPa. Interestingly, a new emission peak fitted by the orange curve appears at this pressure point, and it is located at the lower-energy side than the X^0 emission of individual MoSe$_2$ and WSe$_2$. On the other hand, the interlayer exciton emission (3D exciton) continues to weaken under pressure and vanishes above 2.43 GPa. Inset in Figure 2a shows the images of the 3D exciton emissions at 10 times magnification with pressures ranging from 0 to 2.43 GPa. As guided by black dashed line, the evolution of 3D interlayer exciton emission also experiences a transformation from linear blue-shifts to red-shifts with the increasing pressure. The whole PL of MoSe$_2$−WSe$_2$ HS also attenuates and finally diminishes to the background noise level upon continuous pressurizing (Figure S4). The widths of the excitons peaks are observed to broaden with increasing pressure, which may be partly ascribed to the inhomogeneity of pressure arising from the solidification of the pressure medium.

Before analyzing the behaviors of 2D and 3D excitons in HS, we clarify the high-pressure behaviors of excitons in separate monolayer WSe$_2$ and MoSe$_2$. As shown in Figure 2e,f, the emissions of both X^0 and X$^-$ components in the monolayer WSe$_2$ exhibit a linear blue-shift before 2.43 GPa and turn to red-shift at pressure of 2.43 GPa and above. The energy evolution of X^0 versus pressure can be expressed by $E_g[X^0(WSe_2)_{mono}] = 1.656 + 0.009P$ ($P < 2.43$ GPa) and $E_g[X^0(WSe_2)_{mono}] = 1.687 − 0.001P$ ($P \geq 2.43$ GPa), where E_g represents the exciton energy and P represents the pressure, respectively. Likewise, the energy evolution of X$^-$ emission is expressed as $E_g[X^-(WSe_2)_{mono}] = 1.642 + 0.008P$ ($P < 2.43$ GPa) and $E_g[X^-(WSe_2)_{mono}] = 1.667 − 0.003P$ ($P \geq 2.43$ GPa). The turning point at 2.43 GPa reflects a pressure-induced conduction band K−Λ crossing of monolayer WSe$_2$, i.e., the X^0 and X$^-$ excitons lie in direct K−K interband transition below 2.43 GPa, and then switch to indirect Λ−K interband transition above 2.43 GPa, which has been convinced by both experiments and theoretical simulations.[19,40] For monolayer MoSe$_2$, pressure-induced conduction band K−Λ crossover leading to its direct band gap to indirect band gap transition occurs at 3.7 GPa.[20] Its X^0 emissions show a blue-shift with pressure and a novel X^0 split peak emerges above 3.7 GPa, as shown in Figure 2c,d, These two energy evolutions can be expressed by $E_g[X^0(MoSe_2)_{mono}] = 1.589 + 0.007P − 5.867 \times 10^{-5}P^2$ and $E_g[X^0(MoSe_2)_{mono}$ split$] = 1.618 + 7.365 \times 10^{-4}P$, respectively. The energy evolution of X$^-$ emission is described as $E_g[X^-(MoSe_2)_{mono}] = 1.538 + 0.005P$. The original X^0 emission exists in the whole pressure ranges and the X$^-$ emission is ascribed to K−K transitions, whereas the novel X^0 split emission is derived from the Λ−K interband transition.

Now, we turn back to the evolutions of the 3D interlayer and 2D intralayer excitons in MoSe$_2$−WSe$_2$ HS under compression.
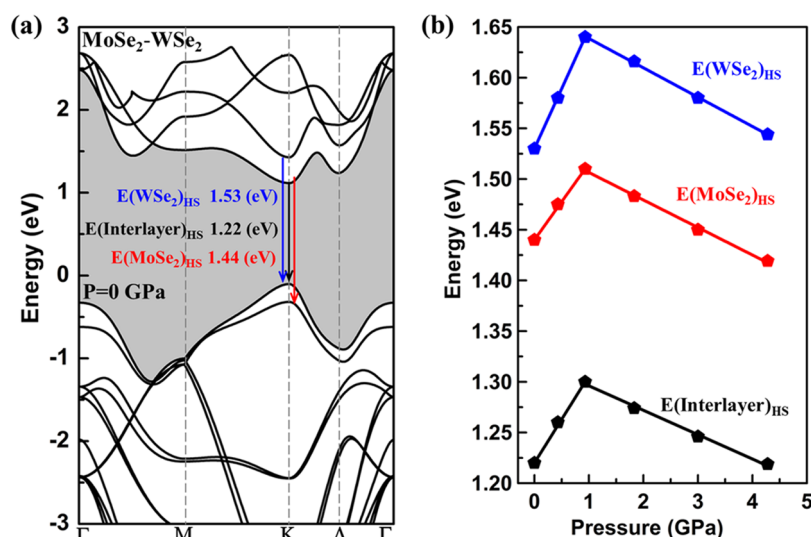
Figure 3. (a) Calculated band structure of MoSe$_2$−WSe$_2$ HS at 0 GPa. (b) Calculated energies for three optical transitions as a function of pressure.

According to Figure 2b, the X^0 emission of WSe$_2$ in HS exhibits a sectionalized linear shift versus pressure with the equation $E_g[X^0(WSe_2)_{HS}] = 1.652 + 0.011P$ ($P < 2.43$ GPa) and $E_g[X^0(WSe_2)_{HS}] = 1.686 − 0.003P$ ($P \geq 2.43$ GPa). This equation confirms an almost same pressure assignment of state with that of the monolayer WSe$_2$, indicating that the vdW force in HS has a faint influence on the 2D exciton in the contributing WSe$_2$ layer. For the X^0 emission of MoSe$_2$ in HS, the energy shows a blue-shift expressed by $E_g[X^0(MoSe_2)_{HS}] = 1.581 + 0.015P$ ($P \leq 2.43$ GPa); it is also almost the same with that of single-monolayer MoSe$_2$. Notably, a new emission peak appeared above 2.43 GPa, which is assigned to the X$^−$ emissions of MoSe$_2$ in HSs. Because the pressure decreases the interlayer distance between MoSe$_2$ and WSe$_2$ substantially, the interlayer relaxation is enhanced and causes a charging effect leading to the emergence of X$^−$ emissions. A second-order polynomial fit of $E_g[X^−(MoSe_2)_{HS}] = 1.529 + 0.034P − 0.005P^2$ ($P \geq 2.43$ GPa) can be applied to describe the pressure dependence of X$^−$ emissions peaks of MoSe$_2$ in HS's at high pressure. There is an inflexion at 3.4 GPa, which is very close to the pressure point where pressure-induced K−Λ crossing appears in the monolayer MoSe$_2$. The energy discrepancy between X$^−$ and X^0 excitons emissions of MoSe$_2$ in HSs is due to trion dissociation energy. Thus, the enhanced interlayer coupling in hydrostatic pressure conditions opens a door for further renormalization of the 2D excitonic system. Besides, because the asymmetric character of the X$^+$ exciton emission in WSe$_2$ was suppressed, it provides a new approach to induce the n-type doping for monolayer TMDs family under hydrostatic pressure without introducing any impurities into the system.

The 3D interlayer exciton emissions exhibited linear blue-shifts below 1.43 GPa, turned to red-shift, and then vanished quickly above 2.43 GPa; similar to the 2D excitons of WSe$_2$, the fitted equation can be expressed as $E_g[(interlayer)_{HS}] = 1.357 + 0.02P$ ($P \leq 1.43$ GPa) and $E_g[(interlayer)_{HS}] = 1.41 − 0.018P$ ($P > 1.43$ GPa). Disappearance of the 3D interlayer exciton emission under compression suggested a dimensional transformation from 3D to 2D excitonic system. That is to say, because 3D exciton is short-lived compared with 2D excitons under hydrostatic pressure, a dimension-modulated process involving a cycle of 2D−3D−2D excitonic system is achieved here. Based on the aforementioned pressure-induced PL

emission transitions in the monolayer MoSe$_2$ and WSe$_2$, it known that their band gap are renormalized leading to the conduction band K−Λ crossover. The similar symmetry of MoSe$_2$ and WSe$_2$ endows the heterostructure with a similar change as homostructural stacking, and similar renormalization of energy band in HS may be achieved.[19,41,42] Upon application of high pressure, the narrowed longitudinal distance between K point and Λ point in valence band maximum (VBM) would be shortened rapidly, leading to a prior conduction band K−Λ crossover in HS.

To confirm our speculation, density functional theory (DFT) calculations are employed to calculate the band structure of MoSe$_2$−WSe$_2$ HS using the QUANTUM ESPRESSO code,[43] the details are provided in Experimental Methods. It is known that stacking order may affect its band structure, according to the previous studies, so we choose the most appropriate AB stacking order of MoSe$_2$−WSe$_2$ HS for calculation.[44] The calculation results are shown in Figure 3; the HS has a direct band gap at K point, where the CBM is localized in the MoSe$_2$ layer and the VBM is localized in the WSe$_2$ layer. The direct optical transition is displayed by a black arrow corresponding to the 3D interlayer exciton emission. According to the analysis of orbital character at K point, the status of HS retains the individual monolayer character,[39,45] where blue and red arrows represent the transitions in orbitals contributions from WSe$_2$ and MoSe$_2$, respectively. These two transitions reflect the 2D intralayer excitons and trion emissions in contributing monolayers. The energy of the K valley increases with increase in pressure, whereas the Λ valley shows a diverse behavior until they converge to the same value (see Figure S5), i.e., it exhibits a pressure-induced K−Λ crossing process. With further compression, the energy of the Λ valley keeps dropping and becomes much lower than that of the K valley, during which the direct K−K point transitions transform into an indirect Λ−K point transitions. Therefore, all of the three optical transitions are modified largely by pressure.

The calculated energies for the three optical transitions as a function of pressure are shown in Figure 3b. As described above, there are distinct turning points in the energy evolutions of all of the three optical transitions as a function of pressure, from the initial linear blue-shift turns into a red-shift afterward. It is in good agreement with that of the experimental 3D
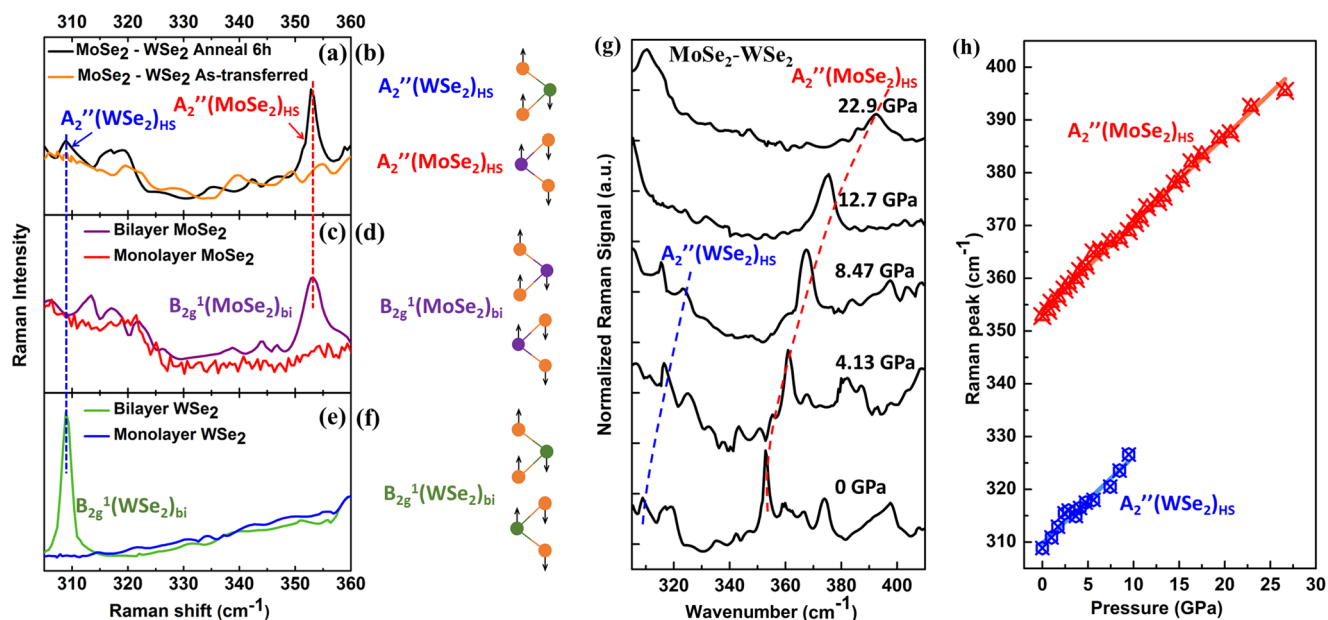
Figure 4. Raman spectra (a) and schematics (b) for A_2'' modes in $MoSe_2$−WSe_2 heterobilayer; (c) and (d) for B_{2g}^1 mode in Bernal-stacked bilayer $MoSe_2$; (e) and (f) for B_{2g}^1 mode in Bernal-stacked bilayer WSe_2. (g) Raman spectra of A_2'' vibrational modes of $MoSe_2$ and WSe_2 in HS versus pressure. The dashed lines are guides to the eye. (h) Pressure dependence of Raman frequencies for A_2'' modes during compression, color-coded by blue (A_2'' mode of WSe_2 in the HS) and red (A_2'' mode of $MoSe_2$ in the HS).
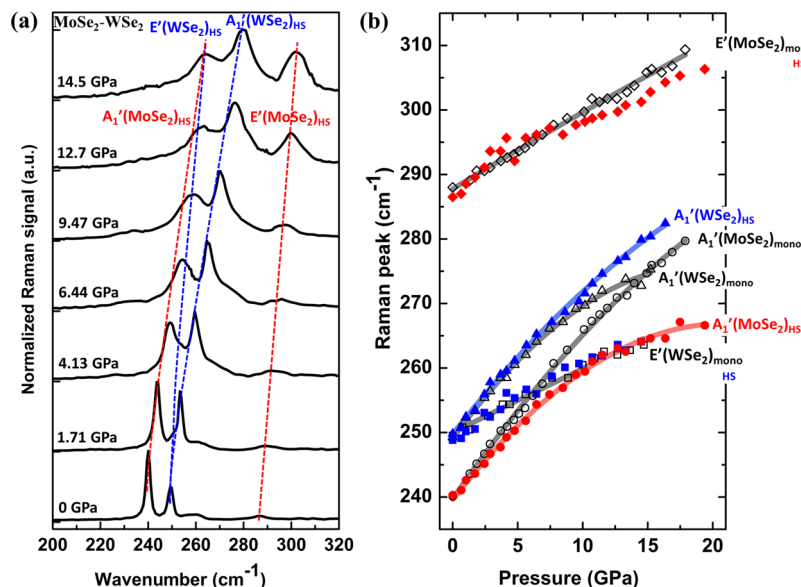
Figure 5. (a) Raman spectra of $MoSe_2$−WSe_2 HS versus pressure. The dashed lines are guides to the eye. (b) Raman frequencies of the E_1' and A_1' vibration modes at a series of pressures, color-coded by blue (WSe_2 in the HS), red ($MoSe_2$ in the HS), and black (both in the monolayers).

interlayer exciton evolution. The turning points for X^0 exciton emissions of WSe_2 and $MoSe_2$ in the HS here appear a bit earlier compared with the experimental observations, this discrepancy is due to the fact that the experimentally fabricated HS may process a low-symmetry stacking configuration and a mismatched atomic alignment, whereas the AB stacking order used in the simulation has a perfect symmetry, which may not match with the experimental case. However, it reveals the intrinsic mechanism of controllable modulation of excitons and trions, which is helpful for developing flexible excitonic devices and provides a promising platform for exploring new excitonic phenomena.

Apart from the electronic structure transitions of HS under pressure, its lattice structural variation can be judged by high-pressure Raman spectra. As shown in Figure 4, there are two obvious Raman peaks for annealed HS located at 352.8 and 308.8 cm^{-1}. A comparison of the Bernal-stacked bilayer $MoSe_2$ and WSe_2 samples (Figure 4c−f) showed that they are close to the B_{2g}^1 modes of the bilayer $MoSe_2$ and WSe_2 emerging at ∼353.3 and 309 cm^{-1}. The B_{2g}^1 mode is regarded as a characteristic feature to distinguish monolayer from other few layers because its equivalent mode in monolayers $MoSe_2$ and WSe_2 are Raman inactive and denoted as the A_2'' mode. On these basis, the 352.8 and 308.8 cm^{-1} vibrations in HS were assigned to the A_2'' modes of $MoSe_2$ and WSe_2 in the vdW HS,

and these A_2'' modes of the annealed HS are activated by a finite restoring force existing between the two-component layers. Thus, from the renormalized vibrational spectra, we believe the spotty-coupled HS turns into a true 3D heterobilayer system in annealed HS.

As pressure can effectively reduce the interlayer distance and strengthen the interlayer coupling and restoring force, the A_2'' peaks gives a blue-shift during compression, accompanied by peak broadening. The shifting corresponding to the $MoSe_2$ and WSe_2 in HS are 1.86 and 1.64 cm^{-1} GPa^{-1}, respectively, and results in 42.7 cm^{-1} shifts from 0 to 26.82 GPa for $MoSe_2$ and 17.8 cm^{-1} shifts from 0 to 9.47 GPa for WSe_2. Therefore, the A_2'' modes of $MoSe_2$ and WSe_2 in HS observed in our research can be used as a sensitive probe to investigate the interlayer interactions existing in van der Waals materials.

For other normal vibrations, namely the out-of-plane A_1' and in-plane E' vibrational modes of HS, a blue-shift is observed upon compression. For single-monolayer WSe_2, the pressurization can stiffen its Raman response and causes A_1' and E' vibrations to go apart; obviously, finally the A_1' mode vibrational frequency is about 10 cm^{-1} higher than the E' mode frequency at 15 GPa. For monolayer $MoSe_2$ on the other hand, its A_1' mode vibrational frequency is about 30 cm^{-1} lower than that of the E' mode vibrational frequency at 15 GPa. Moreover, though the A_1' mode of $MoSe_2$ vibration is slower than that of WSe_2 at ambient pressure, a higher pressure coefficient of $MoSe_2$ makes these two A_1' modes cross together up to 15 GPa. For annealed HS, it is noticed that the stiffer A_1' mode of WSe_2 [$A_1'(WSe_2)_{HS}$] is pushed up and the softer A_1' mode of $MoSe_2$ [$A_1'(MoSe_2)_{HS}$] is pushed down, which shows quite different pressure evolved paths compared with individual monolayers. However, the E' modes of annealed HS are almost the same with those of the individual monolayers, exhibiting a linear pressure dependence. All of the vibrational modes can be easily distinguished from each other (Figure 5), and the details on identification and peak fitting of these Raman peaks are provided in Figure S6.

In the absence of external pressure, the A_1' modes of the two layers in HS vibrate separately and are same with that of monolayer $MoSe_2$ and WSe_2, though the two layers have coupled together after annealing. However, the annealing-induced coupling is weak to an extent. The interlayer coupling is strengthened when an external pressure is introduced. Then, the A_1' vibrations of the two layers in HS will switch to two coherent vibration modes where the Se atoms in both WSe_2 and $MoSe_2$ layers move in concert, with one vibrating in phase and the other vibrating 180° out of phase (shown Figure S8). The stiffened $A_1'(WSe_2)_{HS}$ mode compared to that of individual WSe_2 monolayer $A_1'(WSe_2)_{mono}$ originates from the Se atoms vibrating along the opposite direction in the coherent in-phase modes, whereas the softened $A_1'(MoSe_2)_{HS}$ mode comes from the Se vibrations in consistent direction in the coherent out-of-phase modes.[46] As the pressure increases, the distance reduces further between the two layers and interlayer coupling is enhanced. The renormalization of these two coherent $A_1'_{HS}$ vibrational modes becomes prominent. On the contrary, the in-plane E' modes of the two layers are not coupled with each other even at high pressures, indicating that the intraplane W—Se or Mo—Se covalent bonds are less influenced. These results prove that the three-dimensional vibrational A_2'' modes in HS, as well as the degree of A_1' mode stiffening or softening offer a possible way to evaluate the interlayer coupling interactions in the HS's system.

In conclusion, we fabricated a $MoSe_2$—WSe_2 HS through mechanical exfoliation and vacuum annealing treatment, and high-pressure PL and Raman spectra of the annealed HS were measured in diamond anvil cell. The interlayer coupling was enforced externally with vacuum annealing, leading to a crossover in the electronic structure and lattice vibration from a spotty-coupled status toward a true coupled heterobilayer status. The 3D interlayer exciton is observed in the PL spectrum, and coupled A_2'' vibrations of WSe_2 and $MoSe_2$ are detected in Raman spectrum. Hydrostatic pressure enforced the interlayer coupling further; evidently, a pressure-induced K—Λ crossing process was found and the 3D interlayer exciton experienced a turn from blue-shift to red-shift upon compression and finally diminished to the background noise at about 2.43 GPa, only leaving 2D intralayer excitons of WSe_2 and $MoSe_2$. This coupling-assisted renormalization of electronical system disclosed a cycle of 2D−3D−2D excitonic evolution. The pressure-induced lattice vibrational renormalization represents as linear stiffness of A_2'' mode of WSe_2 and $MoSe_2$ in HS, and coherency of out-of-plane A_1' vibrations of WSe_2 and $MoSe_2$ in HS. As the pressure can decrease the interlayer distance more effectively than thermal treatment, the interlayer coupling effect is modulated to a great extent. It provides an excellent strategy for exploring the coupling-assisted renormalization of excitonic and vibrational system in TMD van der Waals HS. Overall, our work offers the fundamental understanding of coupling-assisted renormalization and gives a convenient way to probe the interlayer coupling intensity, which provides access to design future optoelectronic devices performance.

■ EXPERIMENTAL METHODS

Sample Preparation and Characterizations. $MoSe_2$ and WSe_2 flakes first were mechanically exfoliated from the bulk crystals onto clear and flexible poly(dimethylsiloxane) (Gel Film) substrates using adhesive tapes to achieve the monolayer samples. Optical contrasts through an optical microscope, photoluminescence (PL), and Raman measurements (Figure 1d,e) indicated the good quality of exfoliated monolayer crystals. Afterward, a monolayer $MoSe_2$ was transferred onto a diamond anvil surface in the sample chamber via a micromanipulator. Then, a WSe_2 monolayer flake was precisely transferred onto the $MoSe_2$ flake (Figure S1). The heterostructure flake is finally thermally annealed at 120 °C for 6 h under a vacuum environment below a base pressure of about 0.133 Pa.

A series of high-pressure experiments were performed using a symmetric diamond anvil cells (DAC) with a pair of 300 μm culet anvils. A T301 stainless steel gasket was preindented to reduce its thickness from 250 to 50 μm and subsequently drilled in the center to form a hole of 160 μm diameter. Measurement of the pressure of the sample chamber in DAC was achieved by collecting ruby fluorescence spectra from ruby spheres loaded in the chamber. Inert argon as pressure transmission medium (PTM) was compressively loaded in the sample chamber to offer a continuous hydrostatic pressure applied on the samples.

Raman and PL measurements were carried out using a micro-Raman spectrometer (Horiba-HR-Evolution) equipped with a solid-state green laser (λ = 532 nm) in a back-scattering configuration. The PL signal was dispersed by a 600 g mm^{-1} grating and the Raman signal was dispersed by an 1800 g mm^{-1} grating. The laser power applied on the surface of the sample

was set to be no more than 0.5 mW to avoid the probable damage from heating or oxidizing under exposure. The Gaussian spot diameter used in the fluorescence measurement system is about 1 μm.

Theoretical Calculations. The calculations of the energy band of $MoSe_2$–WSe_2 heterostructure (HS) at different pressures are performed using the QUANTUM ESPRESSO code, within the density functional theory (DFT). Perdew–Burke–Ernzerhof of generalized gradient approximation functional with the exchange–correlation functional was used as the type of pseudopotential during the whole computational procedure. The AB stacking order is adopted for our model systems. The norm-conserving ultrasoft with energy (charge density) cutoff up to 60 Ry (600 Ry) is employed in this work. The first Brillouin zone is sampled with a $20 \times 20 \times 1$ Monkhorst–Pack grid. The vacuum region thickness is greater than 25 Å. The structures are relaxed when the forces exerted on the atoms are less than 1×10^{-7} eV Å^{-1}. To obtain a good accuracy of calculated results, the self-consistent field was set to be $<1 \times 10^{-9}$ eV Å^{-1}. The hydrostatic pressure applied on HS was modeled by calculating the ease of compression along the x-, y-, and z-direction. The force constants were calculated with a unit cell. Despite the fact that the unit cell could not exactly simulate the large supercell of the periodic structure in an experimentally fabricated HS and the AB stacking order used in the simulation has a perfect symmetry that may not match with the experimental case, the calculation still convincingly reveals the intrinsic mechanism of controllable modulation of energy band observed in the experiment.

ASSOCIATED CONTENT

Ⓢ Supporting Information

The Supporting Information is available free of charge on the ACS Publications website at DOI: 10.1021/acs.jpcc.8b01453.

Schematic of the $MoSe_2$–WSe_2 heterobilayers preparation on a diamond substrate; schematic diagram of the DAC; PL intensity of HS and monolayers; band structures of HS at different pressures; Lorentzian fittings for normalized Raman spectra of HS at different pressures; selected experimental Raman spectra of monolayer WSe_2 and $MoSe_2$ at different pressures; the schematics of the coherent in-phase and out-of-phase modes (PDF)

AUTHOR INFORMATION

Corresponding Authors
*E-mail: lifangfei@jlu.edu.cn. Tel: +8643185168881. Fax: +8643185168881 (F.L.).
*E-mail: zhouqiang@jlu.edu.cn (Q.Z.).
ORCID Ⓞ
Fangfei Li: 0000-0002-0342-3872
Tian Cui: 0000-0002-9664-848X

Notes

The authors declare no competing financial interest.

ACKNOWLEDGMENTS

REFERENCES

(1) Tongay, S.; Suh, J.; Ataca, C.; Fan, W.; Luce, A.; Kang, J. S.; Liu, J.; Ko, C.; Raghunathanan, R.; Zhou, J.; et al. Defects Activated Photoluminescence in Two-Dimensional Semiconductors: Interplay Between Bound, Charged, and Free Excitons. *Sci. Rep.* **2013**, *3*, No. 2657.

(2) Lu, X.; Utama, M. I. B.; Lin, J. H.; Gong, X.; Zhang, J.; Zhao, Y. Y.; Pantelides, S. T.; Wang, J. X.; Dong, Z. L.; Liu, Z.; et al. Large-Area Synthesis of Monolayer and Few-Layer $MoSe_2$ Films on SiO_2 Substrates. *Nano Lett.* **2014**, *14*, 2419–2425.

(3) Xia, F. N.; Wang, H.; Xiao, D.; Dubey, M.; Ramasubramaniam, A. Two-Dimensional Material Nanophotonics. *Nat. Photonics* **2014**, *8*, 899–907.

(4) Fan, X.; Chang, C. H.; Zheng, W. T.; Kuo, J. L.; Singh, D. J. The Electronic Properties of Single-Layer and Multilayer MoS_2 under High Pressure. *J. Phys. Chem. C* **2015**, *119*, 10189–10196.

(5) Huang, S.; Ling, X.; Liang, L. B.; Kong, J.; Terrones, H.; Meunier, V.; Dresselhaus, M. S. Probing the Interlayer Coupling of Twisted Bilayer MoS_2 Using Photoluminescence Spectroscopy. *Nano Lett.* **2014**, *14*, 5500–5508.

(6) Zhou, K. G.; Withers, F.; Cao, Y.; Hu, S.; Yu, G. L.; Casiraghi, C. Raman Modes of MoS2 Used as Fingerprint of van der Waals Interactions in 2-D Crystal-Based Heterostructures. *ACS Nano* **2014**, *8*, 9914–9924.

(7) Mak, K. F.; Lee, C.; Hone, J.; Shan, J.; Heinz, T. F. Atomically Thin MoS_2: A New Direct-Gap Semiconductor. *Phys. Rev. Lett.* **2010**, *105*, No. 136805.

(8) Zhang, Y.; Chang, T. R.; Zhou, B.; Cui, Y. T.; Yan, H.; Liu, Z.; Schmitt, F.; Lee, J.; Moore, R.; Chen, Y.; et al. Direct Observation of the Transition From Indirect to Direct Bandgap in Atomically Thin Epitaxial $MoSe_2$. *Nat. Nanotechnol.* **2014**, *9*, 111–115.

(9) Zhang, W.; Huang, J.; Chen, C.; Chang, Y.; Cheng, Y.; Li, L. High-Gain Phototransistors Based on a CVD MoS_2 Monolayer. *Adv. Mater.* **2013**, *25*, 3456–3461.

(10) Allain, A.; Kis, A. Electron and Hole Mobilities in Single-Layer WSe_2. *ACS Nano* **2014**, *8*, 7180–7185.

(11) Ross, J. S.; Klement, P.; Jones, A. M.; Ghimire, N. J.; Yan, J.; Mandrus, D. G.; Taniguchi, T.; Watanabe, K.; Kitamura, K.; Yao, W.; et al. Electrically Tunable Excitonic Light-Emitting Diodes Based on Monolayer WSe_2 p-n Junctions. *Nat. Nanotechnol.* **2014**, *9*, 268–272.

(12) Sundaram, R. S.; Engel, M.; Lombardo, A.; Krupke, R.; Ferrari, A. C.; Avouris, P.; Steiner, M. Electroluminescence in Single Layer MoS_2. *Nano Lett.* **2013**, *13*, 1416–1421.

(13) Eda, G.; Yamaguchi, H.; Voiry, D.; Fujita, T.; Chen, M. W.; Chhowalla, M. Photoluminescence from Chemically Exfoliated MoS_2. *Nano Lett.* **2011**, *11*, 5111–5116.

(14) Ganatra, R.; Zhang, Q. Few-Layer MoS2: A Promising Layered Semiconductor. *ACS Nano* **2014**, *8*, 4074–4099.

(15) Najmaei, S.; Zou, X. L.; Er, D. Q.; Li, J. W.; Jin, Z. H.; Gao, W. L.; Zhang, Q.; Park, S.; Ge, L.; Lei, S.; et al. Tailoring the Physical Properties of Molybdenum Disulfide Monolayers by Control of Interfacial Chemistry. *Nano Lett.* **2014**, *14*, 1354–1361.

(16) Mak, K. F.; He, K. L.; Lee, C.; Lee, G. H.; Hone, J.; Heinz, T. F.; Shan, J. Tightly Bound Trions in Monolayer MoS_2. *Nat. Mater.* **2013**, *12*, 207–211.

(17) Ross, J. S.; Wu, S. F.; Yu, H. Y.; Ghimire, N. J.; Jones, A. M.; Aivazian, G.; Yan, J. Q.; Mandrus, D. G.; Xiao, D.; Yao, W.; et al. Electrical Control of Neutral and Charged Excitons in a Monolayer Semiconductor. *Nat. Commun.* **2013**, *4*, No. 1474.

(18) Nayak, A. P.; Pandey, T.; Voiry, D.; Liu, J.; Moran, S. T.; Sharma, A.; Tan, C.; Chen, C. H.; Li, L. J.; Chhowalla, M.; Akinwande, D.; et al. Pressure-Dependent Optical and Vibrational Properties of Monolayer Molybdenum Disulfide. *Nano Lett.* **2015**, *15*, 346−353.

(19) Ye, Y.; Dou, X. M.; Ding, K.; Jiang, D. S.; Yang, F. H.; Sun, B. Q. Pressure-Induced K-Λ Crossing in Monolayer WSe_2. *Nanoscale* **2016**, *8*, 10843−10848.

(20) Fu, X.; Li, F.; Lin, J.; Gong, Y.; Huang, X.; Huang, Y.; Han, B.; Zhou, Q.; Cui, T. Pressure-Dependent Light Emission of Charged and Neutral Excitons in Monolayer $MoSe_2$. *J. Phys. Chem. Lett.* **2017**, *8*, 3556−3563.

(21) Xiao, D.; Liu, G. B.; Feng, W.; Xu, X.; Yao, W. Coupled Spin and Valley Physics in Monolayers of MoS2 and Other Group-VI Dichalcogenides. *Phys. Rev. Lett.* **2012**, *108*, No. 196802.

(22) Cao, T.; Wang, G.; Han, W.; Ye, H.; Zhu, C.; Shi, J.; Niu, Q.; Tan, P.; Wang, E.; Liu, B.; et al. Valley-Selective Circular Dichroism of Monolayer Molybdenum Disulfide. *Nat. Commun.* **2012**, *3*, No. 887.

(23) Zeng, H.; Dai, J. F.; Yao, W.; Xiao, D.; Cui, X. D. Valley Polarization in MoS_2 Monolayers by Optical Pumping. *Nat. Nanotechnol.* **2012**, *7*, 490−493.

(24) Mak, K. F.; He, K.; Shan, J.; Heinz, T. F. Control of Valley Polarization in Monolayer MoS_2 by Optical Helicity. *Nat. Nanotechnol.* **2012**, *7*, 494−498.

(25) Jones, A. M.; Yu, H.; Ghimire, N. J.; Wu, S.; Aivazian, G.; Ross, J. S.; Zhao, B.; Yan, J.; Mandrus, D. G.; Xiao, D.; et al. Optical Generation of Excitonic Valley Coherence in Monolayer WSe_2. *Nat. Nanotechnol.* **2013**, *8*, 634−638.

(26) Gong, Z.; Liu, G. B.; Yu, H.; Xiao, D.; Cui, X.; Xu, X.; Yao, W. Magnetoelectric Effects and Valley-Controlled Spin Quantum Gates in Transition Metal Dichalcogenide Bilayers. *Nat. Commun.* **2013**, *4*, No. 2053.

(27) Jones, A. M.; Yu, H.; Ross, J. S.; Klement, P.; Ghimire, N. J.; Yan, J.; Mandrus, D. G.; Yao, W.; Xu, X. D. Spin-layer Locking Effects in Optical Orientation of Exciton Spin in Bilayer WSe_2. *Nat. Phys.* **2014**, *10*, 130−134.

(28) Rivera, P.; Schaibley, J. R.; Jones, A. M.; Ross, J. S.; Wu, S.; Aivazian, G.; Klement, P.; Ghimire, N. J.; Yan, J.; Mandrus, D. G.; et al. Observation of Long-Lived Interlayer Excitons in Monolayer $MoSe_2$-WSe_2 Heterostructures. *Nat. Commun.* **2015**, *6*, No. 6242.

(29) Shi, J.; Liu, M.; Wen, J.; Ren, X.; Zhou, X.; Ji, Q.; Ma, D.; Zhang, Y.; Jin, C.; Chen, H.; et al. All Chemical Vapor Deposition Synthesis and Intrinsic Bandgap Observation of MoS_2/Graphene Heterostructures. *Adv. Mater.* **2015**, *27*, 7086−7092.

(30) Yu, Y.; Hu, S.; Su, L.; Huang, L.; Liu, Y.; Jin, Z.; Purezky, A. A.; Geohegan, D. B.; Kim, K. W.; Zhang, Y.; et al. Equally Efficient Interlayer Exciton Relaxation and Improved Absorption in Epitaxial and Nonepitaxial MoS_2/WS_2 Heterostructures. *Nano Lett.* **2015**, *15*, 486−491.

(31) Lu, X.; Utama, M. I. B.; Lin, J. H.; Luo, X.; Zhao, Y. Y.; Zhang, J.; Pantelides, S. T.; Zhou, W.; Quek, S. Y.; Xiong, Q. H. Rapid and Nondestructive Identification of Polytypism and Stacking Sequences in Few-Layer Molybdenum Diselenide by Raman Spectroscopy. *Adv. Mater.* **2015**, *27*, 4502−4508.

(32) Luo, X.; Zhao, Y.; Zhang, J.; Toh, M.; Kloc, C.; Xiong, Q.; Quek, S. Y. Effects of Lower Symmetry and Dimensionality on Raman Spectra in Two-dimensional WSe_2. *Phys. Rev. B* **2013**, *88*, No. 195313.

(33) Tonndorf, P.; Schmidt, R.; Bottger, P.; Zhang, X.; Borner, J.; Liebig, A.; Albrecht, M.; Kloc, C.; Gordan, O.; Zahn, D. R. T.; et al. Photoluminescence Emission and Raman Response of Monolayer MoS_2, $MoSe_2$, and WSe_2. *Opt. Express* **2013**, *21*, 4908−4916.

(34) Zhang, M.; Wu, J.; Zhu, Y.; Dumcenco, D. O.; Hong, J.; Mao, N.; Deng, S.; Chen, Y.; Yang, Y.; Jin, C.; et al. Two-Dimensional Molybdenum Tungsten Diselenide Alloys: Photoluminescence, Raman Scattering, and Electrical Transport. *ACS Nano* **2014**, *8*, 7130.

(35) Nayak, A. P.; Bhattacharyya, S.; Zhu, J.; Liu, J.; Wu, X.; Pandey, T.; Jin, C.; Singh, A. K.; Akinwande, D.; Lin, J. F. Pressure-Induced Semiconducting to Metallic Transition in Multilayered Molybdenum Disulfide. *Nat. Commun.* **2014**, *5*, No. 3731.

(36) Pandey, T.; Nayak, A. P.; Liu, J.; Moran, S. T.; Kim, J. S.; Li, L. J.; Lin, J. F.; Akinwande, D.; Singh, A. K. Pressure-Induced Charge Transfer Doping of Monolayer Graphene/MoS2 Heterostructure. *Small* **2016**, *12*, 4063−4069.

(37) Castellanos-Gomez, A.; Buscema, M.; Molenaar, R.; Singh, V.; Janssen, L.; van der Zant, H. S. J.; Steele, G. A. Deterministic Transfer of Two-Dimensional Materials by All-Dry Viscoelastic Stamping. *2D Mater.* **2014**, *1*, No. 011002.

(38) Castellanos-Gomez, A.; Vicarelli, L.; Prada, E.; Island, J. O.; Narasimha-Acharya, K. L.; Blanter, S. I.; Groenendijk, D. J.; Buscema, M.; Steele, G. A.; Alvarez, J. V.; et al. Isolation and Characterization of Few-Layer Black Phosphorus. *2D Mater.* **2014**, *1*, No. 025001.

(39) Tongay, S.; Fan, W.; Kang, J.; Park, J.; Koldemir, U.; Suh, J.; Narang, D. S.; Liu, K.; Ji, J.; Li, J. B.; et al. Tuning Interlayer Coupling in Large-Area Heterostructures with CVD-Grown MoS2 and WS2 Monolayers. *Nano Lett.* **2014**, *14*, 3185−3190.

(40) Gong, Y. B.; Zhou, Q.; Huang, X. L.; Han, B.; Fu, X. P.; Gao, H. X.; Li, F. F.; Cui, T. Pressure-Induced Photoluminescence Adjustment and Lattice Disorder in Monolayer WSe_2. *ChemNanoMat* **2017**, *3*, 238−244.

(41) Desai, S. B.; Seol, G.; Kang, J. S.; Fang, H.; Battaglia, C.; Kapadia, R.; Ager, J. W.; Guo, J.; Javey, A. Strain-Induced Indirect to Direct Bandgap Transition in Multilayer WSe_2. *Nano Lett.* **2014**, *14*, 4592−4597.

(42) Yun, W. S.; Han, S. W.; Hong, S. C.; Kim, I. G.; Lee, J. D. Thickness and Strain Effects on Electronic Structures of Transition Metal Dichalcogenides: 2H-MX2 Semiconductors (M = Mo, W; X = S, Se, Te). *Phys. Rev. B* **2012**, *85*, No. 033305.

(43) Giannozzi, P.; Baroni, S.; Bonini, N.; Calandra, M.; Car, R.; Cavazzoni, C.; Ceresoli, D.; Chiarotti, G. L.; Cococcioni, M.; Dabo, I.; et al. QUANTUM ESPRESSO: a Modular and Open-Source Software Project for Quantum Simulations of Materials. *J. Phys.: Condens. Matter* **2009**, *21*, No. 395502.

(44) Amin, B.; Singh, N.; Schwingenschlogl, U. Heterostructures of Transition Metal Dichalcogenides. *Phys. Rev. B* **2015**, *92*, No. 075439.

(45) Komsal, H.-P.; Krasheninnikov, A. V. Electronic Structures and Optical Properties of Realistic Transition Metal Dichalcogenide Heterostructures from First Principles. *Phys. Rev. B* **2013**, *88*, No. 085318.

(46) Fan, W.; Zhu, X.; Ke, F.; Chen, Y. B.; Dong, K. C.; Ji, J.; Chen, B.; Tongay, S.; Ager, J. W.; Liu, K.; et al. Vibrational Spectrum Renormalization by Enforced Coupling Across the Van Der Waals Gap Between MoS_2 and WS_2 Monolayers. *Phys. Rev. B* **2015**, *92*, No. 241408.